Journal of Computational Acoustics, Vol. 22, No. 2 (2014) 1450002 (23 pages)

DOI: 10.1142/S0218396X14500027

INTERNATIONAL ASSOCIATION
FOR MATHEMATICS AND
COMPUTERS IN SIMULATION

Tracing Three-Dimensional Acoustic Wavefronts in Inhomogeneous, Moving Media

Nikolay A. Zabotin
Department of Electrical, Energy and Computer Engineering and Cooperative Institute for Research in Environmental Sciences, University of Colorado Boulder
Boulder, Colorado 80309, USA
Nikolay.Zabotin@Colorado.edu

Oleg A. Godin
Cooperative Institute for Research in Environmental Sciences University of Colorado Boulder and NOAA/ESRL, Physical Sciences Division
Boulder, Colorado 80305, USA
Oleg.Godin@noaa.gov

Paul C. Sava
Center for Wave Phenomena, Colorado School of Mines
Golden, CO 80401, USA
psava@mines.edu

Liudmila Y. Zabotina
Department of Electrical, Energy and Computer Engineering University of Colorado Boulder
Boulder, Colorado 80309, USA
Liudmila.Zabotina@Colorado.edu

Received 13 September 2013
Accepted 18 November 2013
Published 20 January 2014

We present a numerical implementation of an alternative formulation of the geometrical, or ray, acoustics, where wavefronts rather than rays are the primary objects. Rays are recovered as a by-product of wavefront tracing. The alternative formulation of the geometrical acoustics is motivated, first, by the observation that wavefronts are often more stable than rays at long-range sound propagation, and, second, by a need for computationally efficient modeling of high-frequency acoustic fields in three-dimensionally inhomogeneous, moving or motionless fluids. Wavefronts are found as a finite-difference solution to a system of partial differential equations, which is equivalent to the eikonal equation and is a direct implementation of the intuitive Huygens' wavefront construction. The finite-difference algorithm is an extension of the approach originally developed in the framework of an open source Madagascar project. Benchmark problems, which admit exact, analytic solutions

of the eikonal equation, are formulated and utilized to verify the finite-difference wavefront tracing algorithm. Huygens' wavefront tracing (HWT) is applied to modeling sound propagation in three-dimensionally inhomogeneous ocean and atmosphere.

Keywords: Wavefronts; timefronts; wavefront tracing; moving media; inhomogeneous media; geometrical acoustics; underwater acoustics; infrasound.

1. Introduction

In an underwater acoustics context, it has been established experimentally[1–4] and confirmed by numerical simulations[5–10] that early arrivals of acoustic waves at long-range propagation in the deep ocean are stable and identifiable despite strong perturbations of the ray paths due to sound-speed fluctuations primarily induced by internal gravity waves (IWs). The first observation that strong perturbations of ray trajectories in the ocean do not necessarily engender strong perturbations of signal arrival times resulted from numerical experiments by Palmer *et al.*[11]

The relative stability of the wavefronts takes place because, at any given moment, scattering of the end points of rays resulting from weak perturbations in the refraction index occurs primarily along wavefronts of the unperturbed wave with the same travel time.[12–15] Scattering of the ray end points can be characterized by the anisotropy ratio, defined as the ratio of norms of components of the end points' displacement along and across the unperturbed wavefront. At large propagation ranges, the anisotropy ratio increases as the ratio of the ray length to a representative spatial scale of the refraction index perturbations.[12] Since the end points of rays, which are traced to a fixed eikonal value, lie on the same wavefront, the anisotropy ratio also quantifies the ratio of the ray and wavefront deformations and characterizes the difference in the ray and wavefront stability.

It is wavefronts rather than rays that are typically observed in atmospheric and underwater acoustic experiments. In underwater acoustics, observations with linear vertical arrays of acoustic field due to impulsive sources (as well as sources emitting m-sequences or other known phase-manipulated signals) clearly show how consecutive wavefronts sweep across the arrays, see, e.g. Ref. 4. Without doubt, wavefronts can be equally well visualized in atmospheric acoustics given a relatively dense, multi-element receiver array. Arrival of a signal on an array element indicates a passage of a wavefront through that point; wavefront geometry can be visualized and/or mathematically reconstructed by interpolation between the array elements. On the other hand, "identity" of a ray (its launch angle in the case of a compact sound source) is not manifested in such observations and in fact becomes unpredictable at sufficiently large ranges in underwater waveguides.[6–11]

When wavefronts are much more stable than rays, the traditional approach to numerical implementation of geometrical acoustics, which relies on ray tracing to determine the wavefronts' position, may be counterproductive and sometimes misleading. In particular, this is the case in highly structured (multi-scale) environments such as the ocean with internal waves and "spice" or atmosphere with rapidly changing winds.

A major problem with direct modeling of acoustic wavefronts without solving ray tracing equations (for example, through numerical solution of the eikonal equation) lies in the

eikonal (and acoustic travel time) being a multi-valued function of position. A number of computational approaches to solve the eikonal equation without ray tracing have been proposed.[16–31] Some of these methods are only capable of tracing the wavefront of the earliest, first arrival[16,17,21,24,25,27] and thus are not suitable for acoustic applications in complex multi-scale media. Other methods allow for the eikonal to be multi-valued and, thus, for multiple arrivals.[18,20,22,23,25,26,28–30]

The new algorithm presented in this paper is an extension of Huygens wavefront tracing (HWT)[23,28,32] to three-dimensional (3D) sound propagation in moving media. HWT was originally developed by Sava and Fomel[23,32] for seismic modeling and imaging and extended to moving media by Zabotin *et al.*[28] HWT has the important ability to track multiple arrivals and consists in solving by a finite-difference technique a certain system of partial differential equations, which is equivalent to the eikonal equation. This should be contrasted with wavefront construction using traditional ray tracing, where the eikonal equation is solved by numerically integrating a large number of ordinary differential equations describing individual rays. With the HWT method, each wavefront is generated from the preceding one by finite differences.

The remainder of the paper is organized as follows. Differential and difference equations expressing the Huygens' principle in moving fluids and underlying the new HWT algorithm are derived in Sec. 2. Implementation of the initial conditions and handling of reflecting boundaries in the finite-difference scheme are discussed in Sec. 3. Exact, analytic solutions of the eikonal equation, which are used to benchmark the numerical algorithm, are presented in Sec. 4. Evolution of an underwater acoustic field during passage of a train of nonlinear IWs and long-range propagation in the atmosphere of volcano-generated infrasound are considered in Sec. 5 to illustrate the application of wavefront tracing to problems, where accurate description of 3D refraction and acoustic effects due to background fluid flow are critical. Section 6 summarizes our findings and outlines future development of the HWT algorithm.

2. Mathematical Approach

2.1. *Differential equations*

Consider acoustic rays and wavefronts in a three-dimensionally inhomogeneous fluid with sound speed $c(\mathbf{x})$ and flow velocity $\mathbf{u}(\mathbf{x})$. Parameters of the fluid are smooth functions of position $\mathbf{x} = (x, y, z)$. In geophysical applications, z will be chosen as the vertical Cartesian coordinate. For nondispersive waves (as sound is usually modeled in underwater and atmospheric acoustics), eikonal Ψ, slowness $\mathbf{s} = \nabla\Psi$, ray trajectories, wave front geometry and group velocity[33] $\mathbf{c}_g = \mathbf{u} + cs^{-1}\mathbf{s}$ are independent of wave frequency; the wave vector $\mathbf{k} = \omega\mathbf{s}$ for continuous waves of frequency ω. By definition, the eikonal is constant on the wavefronts. The difference of the eikonal values at any two points on a ray equals the acoustic travel time between these points along the ray.

Let a ray $\mathbf{x} = \mathbf{r}(t, \gamma_1, \gamma_2)$ be parameterized as a function of time t and two parameters $\gamma_{1,2}$ that specify the ray, such as the polar θ and azimuth φ angles that determine direction

of the ray launch from a point source or the position of the launch point on an initial wave front. The set $\{t, \gamma_1, \gamma_2\}$ can be viewed as ray coordinates. In moving fluids, the eikonal equation[33] and differential equations of rays[14,34] can be written as, respectively,

$$\mathbf{s} \cdot \mathbf{u} + sc = 1, \tag{1}$$

$$\frac{d\mathbf{r}}{dt} = \mathbf{u} + c\frac{\mathbf{s}}{s}, \tag{2}$$

$$\frac{ds_\alpha}{dt} = -s\frac{\partial c}{\partial x_\alpha} - \sum_{\beta=1}^{3} s_\beta \frac{\partial u_\beta}{\partial x_\alpha}, \quad \alpha = 1, 2, 3. \tag{3}$$

Here d/dt stands for partial time derivatives taken with $\gamma_{1,2}$ kept constant. Ray equations (2) and (3) are a set of ordinary differential equations, with t being the only independent variable. For derivatives $\mathbf{R}^{(\alpha)} = \partial\mathbf{r}/\partial\gamma_\alpha$ of the ray trajectory with respect to the initial conditions, it is shown in Ref. 14 that the inner product

$$\mathbf{s} \cdot \mathbf{R}^{(\alpha)} = 0 \tag{4}$$

at every point on a ray, if the product is zero at any one point on the ray. We will assume that $\gamma_{1,2}$ are chosen to satisfy the latter condition. For rays emanating from a point source, Eq. (4) holds for any parameterization of the rays provided the fluid is homogeneous in a small vicinity of the source.

To derive equations for wavefronts, we largely follow the original approach of Sava and Fomel.[32] Our goal here is to demonstrate, how such equations can be derived directly from the Huygens' principle. Integrating Eq. (2) over time, one obtains

$$\left|\mathbf{x} - \mathbf{r}(t, \gamma_1, \gamma_2) - \int_t^{t+\varepsilon} \mathbf{u} dt\right|^2 = \left|\int_t^{t+\varepsilon} c\frac{\mathbf{s}}{s} dt\right|^2. \tag{5}$$

This equation describes position $\mathbf{x}$ of point on a virtual acoustic wavefront, which would occur at time $t + \varepsilon$ if a pulse were radiated at the moment t at the point $\mathbf{r}(t, \gamma_1, \gamma_2)$. The virtual wavefront is a sphere with center at $\mathbf{r}$ and radius εc in a homogeneous, motionless medium. For infinitesimal ε, Eq. (5) gives

$$\left|\mathbf{x} - \mathbf{r} - \varepsilon\frac{\mathbf{u}(\mathbf{x}) + \mathbf{u}(\mathbf{r})}{2}\right|^2 = \frac{\varepsilon^2}{4}[c(\mathbf{x}) + c(\mathbf{r})]^2 + O(\varepsilon^4). \tag{6}$$

Virtual wavefronts at time $t+\varepsilon$ are generated for every point $\mathbf{r}$ on the actual wavefront at time t. Dependence on parameters $\gamma_{1,2}$ enters Eqs. (5) and (6) through $\mathbf{r}(t, \gamma_1, \gamma_2)$. According to the Huygens' principle,[35] the actual wavefront at time $t + \varepsilon$ is an envelope of the virtual wavefronts. Point $\mathbf{x}$ on the envelope satisfies Eq. (5) and its derivatives with respect to parameters $\gamma_{1,2}$ (see, e.g. Ref. 36, Sec. 17.3–17.11). Differentiating Eq. (6) with respect to

γ_α, we obtain

$$\left[\mathbf{x}-\mathbf{r}-\varepsilon\frac{\mathbf{u}(\mathbf{x})+\mathbf{u}(\mathbf{r})}{2}\right]\cdot\left(\frac{\partial\mathbf{r}}{\partial\gamma_\alpha}+\frac{\varepsilon}{2}\frac{\partial\mathbf{u}}{\partial\gamma_\alpha}\right)=-\frac{\varepsilon^2}{4}[c(\mathbf{x})+c(\mathbf{r})]\frac{\partial c}{\partial\gamma_\alpha}+O(\varepsilon^3),\quad \alpha=1,2. \tag{7}$$

In the limit $\varepsilon\to 0$, from Eqs. (5) and (7) we obtain differential equations for acoustic wavefronts:

$$\left|\frac{d\mathbf{r}}{dt}-\mathbf{u}\right|^2=c^2, \tag{8}$$

$$\left(\frac{d\mathbf{r}}{dt}-\mathbf{u}\right)\cdot\frac{\partial\mathbf{r}}{\partial\gamma_\alpha}=0,\quad \alpha=1,2, \tag{9}$$

which for two-dimensional (2D) problems reduce to respective equations in Ref. 28. Note that Eq. (9) is equivalent to Eq. (4), which was obtained earlier[14] by different means. Unlike ray equations (2) and (3), Eqs. (8) and (9) comprise a set of simultaneous partial differential equations with three independent variables: t,γ_1 and γ_2.

2.2. *Difference equations*

Introduce a discrete mesh in $\{t,\gamma_1,\gamma_2\}$, with integer indices i,k and j enumerating steps in γ_1,γ_2 and t, respectively. Let $\mathbf{m}=\mathbf{u}/c, a=\varepsilon c$ and $t_{j+1}-t_j=\varepsilon$. Then, neglecting terms of the third- and higher-orders in ε, Eqs. (6) and (7) can be written as the following difference equations:

$$|\mathbf{r}_{j+1}^{i,k}-\mathbf{r}_j^{i,k}-\mathbf{m}_j^{i,k}a_j^{i,k}|^2=(a_j^{i,k})^2, \tag{10}$$

$$\begin{aligned}&(2\mathbf{r}_j^{i,k}-2\mathbf{r}_{j+1}^{i,k}+3\mathbf{m}_j^{i,k}a_j^{i,k}-\mathbf{m}_{j-1}^{i,k}a_{j-1}^{i,k})\\&\qquad\cdot(2\mathbf{r}_j^{i+1,k}-2\mathbf{r}_j^{i-1,k}+\mathbf{m}_j^{i+1,k}a_j^{i+1,k}-\mathbf{m}_j^{i-1,k}a_j^{i-1,k})\\&\quad=2a_j^{i,k}(a_j^{i+1,k}-a_j^{i-1,k}),\end{aligned} \tag{11}$$

$$\begin{aligned}&(2\mathbf{r}_j^{i,k}-2\mathbf{r}_{j+1}^{i,k}+3\mathbf{m}_j^{i,k}a_j^{i,k}-\mathbf{m}_{j-1}^{i,k}a_{j-1}^{i,k})\\&\qquad\cdot(2\mathbf{r}_j^{i,k+1}-2\mathbf{r}_j^{i,k-1}+\mathbf{m}_j^{i,k+1}a_j^{i,k+1}-\mathbf{m}_j^{i,k-1}a_j^{i,k-1})\\&\quad=2a_j^{i,k}(a_j^{i,k+1}-a_j^{i,k-1}).\end{aligned} \tag{12}$$

As is clear from their derivation, Eqs. (10)–(12) are a direct expression of the Huygens' principle.

In the particular case of motionless media ($\mathbf{m}=0$) considered in Ref. 32, Eqs. (11) and (12) reduce to $(\mathbf{r}_j^{i,k}-\mathbf{r}_{j+1}^{i,k})\cdot(\mathbf{r}_j^{i+1,k}-\mathbf{r}_j^{i-1,k})=0.5a_j^{i,k}(a_j^{i+1,k}-a_j^{i-1,k})$ and $(\mathbf{r}_j^{i,k}-\mathbf{r}_{j+1}^{i,k})\cdot(\mathbf{r}_j^{i,k+1}-\mathbf{r}_j^{i,k-1})=0.5a_j^{i,k}(a_j^{i,k+1}-a_j^{i,k-1})$, respectively, and differ from corresponding equations in Ref. 32 by an additional factor of 0.5 in the right-hand side. This difference can be traced back to the fact that not all terms of the second-order in the time step ε were retained in the derivation in Ref. 32.

Using Eqs. (2)–(4), it is straightforward to verify that the solutions of the ray equations satisfy difference equations (10)–(12). This serves as a check of the difference equation validity and also demonstrates that a discrete version of the 3D ray trajectories $\mathbf{r}(t, \gamma_1, \gamma_2)$ can be obtained as a by-product of solving Eqs. (10)–(12) for the wavefronts.

2.3. *Finite-difference scheme*

In solving the difference equations numerically, we found it expedient for $\mathbf{r}_j^{i\pm1,k}$ and $\mathbf{r}_j^{i,k\pm1}$ to mean $\mathbf{r}_j^{i,k} \pm (\mathbf{b}_{\gamma1})_j^{i,k} l$ and $\mathbf{r}_j^{i,k} \pm (\mathbf{b}_{\gamma2})_j^{i,k} l$, respectively, rather than values of $\mathbf{r}$ at the corresponding, globally fixed values of the parameters γ_1 and γ_2. Here, $\mathbf{b}_{\gamma1}$ and $\mathbf{b}_{\gamma2}$ approximate, to first-order in ε, the unit vectors $|\partial\mathbf{r}/\partial\gamma_1|^{-1}\partial\mathbf{r}/\partial\gamma_1$ and $|\partial\mathbf{r}/\partial\gamma_2|^{-1}\partial\mathbf{r}/\partial\gamma_2$, which are tangential to the wavefront, and l is a unit step of the mesh in the tangent plane to the wavefront. According to Eq. (2), the vector $d\mathbf{r}/dt - \mathbf{u}$ is orthogonal to the wavefront. We approximate the wavefront normal as

$$\mathbf{B}_j^{i,k} = \mathbf{r}_j^{i,k} - \mathbf{r}_{j-1}^{i,k} - a_{j-1}^{i,k}\mathbf{m}_{j-1}^{i,k} \tag{13}$$

and, at each grid point, require $(\mathbf{b}_{\gamma1})_j^{i,k}$ and $(\mathbf{b}_{\gamma2})_j^{i,k}$ to be orthogonal to $\mathbf{B}_j^{i,k}$.

With the new meaning of $\mathbf{r}_j^{i\pm1,k}$ and $\mathbf{r}_j^{i,k\pm1}$, the difference equations (11) and (12) become

$$\begin{aligned}(\mathbf{r}_j^{i,k} - \mathbf{r}_{j+1}^{i,k} + \mathbf{m}_j^{i,k} a_j^{i,k}) \cdot (\mathbf{r}_j^{i+1,k} - \mathbf{r}_j^{i-1,k} + a_j^{i+1,k}\mathbf{m}_j^{i+1,k} - a_j^{i-1,k}\mathbf{m}_j^{i-1,k}) \\ = a_j^{i,k}(a_j^{i+1,k} - a_j^{i-1,k}),\end{aligned} \tag{14}$$

$$\begin{aligned}(\mathbf{r}_j^{i,k} - \mathbf{r}_{j+1}^{i,k} + \mathbf{m}_j^{i,k} a_j^{i,k}) \cdot (\mathbf{r}_j^{i,k+1} - \mathbf{r}_j^{i,k-1} + a_j^{i,k+1}\mathbf{m}_j^{i,k+1} - a_j^{i,k-1}\mathbf{m}_j^{i,k-1}) \\ = a_j^{i,k}(a_j^{i,k+1} - a_j^{i,k-1}),\end{aligned} \tag{15}$$

while Eq. (10) remains unchanged. Using Eqs. (2)–(4) and (13), it can be verified that the solutions of the ray equations satisfy difference equations (14) and (15). In 2D problems, the finite-difference scheme (10), (13)–(15) reduces to the scheme we used in Ref. 28. The scheme is first-order accurate in ε. Higher-order accuracy can be achieved, if desired, but it is beyond the scope of the present paper.

A significant advantage of the difference scheme is that, as in the 2D case,[28] the set (10), (14) and (15) admits a simple, explicit solution for $\mathbf{r}_{j+1}^{i,k}$. Thus, the next, $(j+1)$th position of the wavefront on a base ray path i, k is found from coordinates of five points on the previous wavefront j. An analysis shows that the solution of the difference equations (10), (14) and (15) converges to the solution of the differential equations (8) and (9), with the discrepancy decreasing linearly with the step size of the difference scheme.

The finite-difference scheme (10), (14) and (15) has another important advantage when it comes to calculation of the acoustic field amplitude in the geometrical acoustics approximation. The solution $\mathbf{r}_j^{i,k}$ of the difference equations provides finite-difference approximations to the derivatives $d\mathbf{r}/dt, \partial\mathbf{r}/\partial\gamma_1$ and $\partial\mathbf{r}/\partial\gamma_2$ of the ray trajectory. In moving fluids, acoustic pressure amplitude is readily calculated in terms of the local values of these derivatives as well as the flow velocity, sound speed and density of the fluid, see Eq. (5.1.33) in Ref. 33.

3. Scheme Initialization and Sound Reflection

Specification of a wavefront at $j = 1$ serves as the initial condition for the finite-difference scheme (10), (13)–(15). In the case of a point source, we assume that the spatial variation of the sound speed $c(\mathbf{x})$ and the flow velocity $\mathbf{u}(\mathbf{x})$ near the source can be neglected over distances of the order of one step of the scheme. Then, according to Eq. (2),

$$\mathbf{r}_1^{i,k} = \mathbf{x}_0 + \varepsilon c(\mathbf{x}_0)\mathbf{e}_{ik} + \varepsilon \mathbf{u}(\mathbf{x}_0), \quad \mathbf{e}_{ik} = (\sin\vartheta_i \cos\psi_k, \sin\vartheta_i \sin\psi_k, \cos\vartheta_i), \tag{16}$$

where $\mathbf{x}_0$ is the source position, and polar ϑ_i and azimuthal ψ_k angles determine direction of the wave normal.

In stationary (i.e. time-independent) media, boundaries are motionless in the absence of sound, and the normal component of the flow velocity vanishes at the boundary.[33] At sound reflection at a smooth boundary, components of the slowness vector $\mathbf{s}$ tangential to the boundary remain continuous.[33] Then, it follows from Eq. (1) that the tangential components of the group speed $\mathbf{c}_g$ remain continuous on a ray at the reflection point, while the normal component of $\mathbf{c}_g$ changes its sign without changing its magnitude, just as in motionless fluids. This means that the three vectors — tangents to incident and reflected rays and the normal to the boundary at the reflection point — belong to the same plane, and the angle of incidence equals the angle of reflection.

For plane boundaries, handling of the reflection by the finite-difference scheme starts with testing at every step of the scheme if the new position of the wavefront $\mathbf{r}_{j+1}^{i,k}$ and the previous position of the wavefront $\mathbf{r}_j^{i,k}$ appear at different sides of the boundary. If the result of the test is positive, then the point $\mathbf{r}_{j+1}^{i,k}$ is replaced with the point $\tilde{\mathbf{r}}_{j+1}^{i,k}$ symmetrical to the point $\mathbf{r}_{j+1}^{i,k}$ with respect to the plane boundary. This is the next position of the wavefront on the base ray i, k. For the next step of the calculations (described in Sec. 2.3), the previous position of the wavefront $\mathbf{r}_j^{i,k}$ is replaced with an auxiliary point $\tilde{\mathbf{r}}_j^{i,k}$ symmetrical to the point $\mathbf{r}_j^{i,k}$ with respect to the boundary. Reflection at a curved boundary can be handled by approximating the latter with a tangent plane in a small vicinity of the intersection point revealed in the test we just described.

4. Benchmark Problems

To verify numerical wavefront tracing and the underlying HWT algorithm, we set up four benchmark problems. These problems were chosen so that exact, analytic solutions of the eikonal equation can be obtained for point sources.

In motionless, horizontally stratified media, 3D implementation of the HWT algorithm, which is outlined in Secs. 2 and 3, has been verified against the exact, explicit, analytic solutions for wavefronts and timefronts in fluids with $\nabla c = \text{const.}$ and $\nabla c^{-2} = \text{const.}$ The analytic solutions are given by Eqs. (18)–(20) and (22) in Ref. 28. In 3D, the agreement between numerical and analytic solutions was found to be as good as in the 2D case considered in Ref. 28. We do not present here any figures illustrating agreement between 3D

implementation of the HWT algorithm and analytical results for these benchmarks because the figures would be essentially indistinguishable from those published in Ref. 28.

Below, we discuss in detail two other benchmark problems.

4.1. *Moving fluid with linear sound speed and flow velocity profiles*

Consider fluid half-space $z < 0$ with linear dependences

$$c(z) = -\alpha z, \quad \mathbf{u}(z) = ((1-\gamma z)u_0, 0, 0) \tag{17}$$

of the sound speed and background flow velocity on depth z. Here α, γ and u_0 are constants. Let a point sound source be located at the point $(0, 0, z_0), z_0 < 0$. We assume for definiteness that

$$\alpha \geq |\gamma u_0|, \quad \alpha|z_0| > |u_0(1-\gamma z_0)|. \tag{18}$$

Consider a ray, for which the wave normal $\mathbf{n} = \mathbf{s}/s$ makes a grazing angle χ with the xy plane at the source. Then $\mathbf{n} = (\cos\chi\cos\psi, \cos\chi\sin\psi, \sin\chi)$ at $z = z_0$, where $-\pi < \chi \leq \pi$ and the azimuthal angle $\psi, -\pi/2 \leq \psi < \pi/2$ describes the orientation of the projection of the wave normal on the horizontal plane xy. As sound propagates along a ray, the angle between the wave normal and the xy plane changes but the azimuthal angle remains the same.

Under conditions (18), rays with $-\pi < \chi < 0$ have no turning points, and rays with $0 \leq \chi \leq \pi$ have at most one turning point, i.e. a point where vertical components of the wave normal and, hence, group velocity, equal zero. For rays without turning points, $z > z_0$ when $\chi > 0$ and $z < z_0$ when $\chi < 0$. For such rays, their geometry and acoustic travel time from the source are given by the following algebraic equations:

$$\begin{aligned} x(z,\chi,\psi) = \Bigg[& \frac{u_0 z_0(\alpha + \gamma u_0 \cos\chi\cos\psi)}{\alpha^2\sqrt{1-\gamma^2u_0^2\cos^2\psi/\alpha^2}|\cos\chi|}F_1(a,b,z) - \frac{\gamma u_0 F_2(a,b,z)\mathrm{sgn}(\cos\chi)}{\alpha^2\sqrt{1-\gamma^2u_0^2\cos^2\psi/\alpha^2}} \\ & \times\left(t\frac{\alpha z_0}{\cos\chi} - u_0(1-\gamma z_0)\cos\psi\right) \\ & + \frac{(1-\gamma^2u_0^2/\alpha^2)\cos\psi\,\mathrm{sgn}(\cos\chi)}{\sqrt{1-\gamma^2u_0^2\cos^2\psi/\alpha^2}}F_3(a,b,z)\Bigg]\Bigg|_{z=z_-}^{z=z_+}, \end{aligned} \tag{19}$$

$$y(z,\chi,\psi) = \mathrm{sgn}(\cos\chi)\frac{\sin\psi}{\sqrt{1-\gamma^2u_0^2\cos^2\psi/\alpha^2}}F_3(a,b,z)|_{z=z_-}^{z=z_+}, \tag{20}$$

$$\begin{aligned} t(z,\chi) = & \,\mathrm{sgn}(\cos\chi) \\ & \times\left[\frac{\gamma u_0\cos\psi + \alpha\cos^{-1}\chi}{\alpha^2\sqrt{1-\gamma^2u_0^2\cos^2\psi/\alpha^2}}z_0F_1(a,b,z) + \frac{\gamma u_0\cos\psi F_2(a,b,z)}{\alpha^2\sqrt{1-\gamma^2u_0^2\cos^2\psi/\alpha^2}}\right]\Bigg|_{z=z_-}^{z=z_+}. \end{aligned} \tag{21}$$

Here $z_+ = \max(z, z_0), z_- = \min(z, z_0)$,

$$a = \frac{-z_0(\alpha + \gamma u_0 \cos\chi \cos\psi)}{(\alpha - \gamma u_0 \cos\psi \mathrm{sgn}(\cos\chi))|\cos\chi|}, \quad b = \frac{-z_0(\alpha + \gamma u_0 \cos\chi \cos\psi)}{(\alpha + \gamma u_0 \cos\psi \mathrm{sgn}(\cos\chi))|\cos\chi|}, \tag{22}$$

$$F_1(a, b, z) = \frac{-1}{\sqrt{ab}} \ln \frac{2ab + (b-a)z + 2\sqrt{ab}\sqrt{(a+z)(b-z)}}{z}, \tag{23}$$

$$F_2(a, b, z) = -2 \arctan \sqrt{\frac{b-z}{a+z}} \tag{24}$$

and

$$F_3(a, b, z) = -\sqrt{(a+z)(b-z)} - \frac{a-b}{2} \arctan \frac{a-b+2z}{2\sqrt{(a+z)(b-z)}}. \tag{25}$$

Equations (19)–(21) can be viewed as a parametric description of 3D wavefronts and an implicit description of the corresponding timefronts. Equations (19)–(21) follow from the general equations[33] for rays in layered moving media. For the linear sound speed and flow velocity profiles considered here, integrals in the general ray equations[33] can be evaluated in the closed form, leading to Eqs. (23)–(25). At $\psi = 0$, i.e. at sound propagation up- or downstream, Eqs. (19)–(22) reduce to the parametric wavefront equations we employed in the 2D case.[28]

Equations (19)–(21) are not applicable when $\cos\chi = 0$. On rays with $\chi = \pm\pi/2$, there are no turning points, the unit wave normal $\mathbf{n}$ is vertical, and

$$x\left(z, \chi = \pm\frac{\pi}{2}, \psi\right) = \frac{u_0}{\alpha}\left[\left|\ln\frac{z}{z_0}\right| + \gamma|z - z_0|\right], \quad y\left(z, \chi = \pm\frac{\pi}{2}, \psi\right) = 0,$$

$$t\left(z, \chi = \pm\frac{\pi}{2}, \psi\right) = \frac{1}{\alpha}\left|\ln\frac{z}{z_0}\right|. \tag{26}$$

For rays with $\chi > 0$ that have a turning point (it is located at $z = b$), instead of Eqs. (19)–(21), we have

$$\begin{aligned} x(z, \chi, \psi) = {} & \frac{-u_0 z_0(\alpha + \gamma u_0 \cos\chi \cos\psi)}{\alpha^2\sqrt{1 - \gamma^2 u_0^2 \cos^2\psi/\alpha^2}|\cos\chi|}\left[\frac{2\ln(a+b)}{\sqrt{ab}} + F_1(a, b, z) + F_1(a, b, z_0)\right] \\ & + \frac{\gamma u_0 \,\mathrm{sgn}(\cos\chi)}{\alpha^2\sqrt{1 - \gamma^2 u_0^2 \cos^2\psi/\alpha^2}}\left(\frac{\alpha z_0}{\cos\chi} - u_0(1 - \gamma z_0)\cos\psi\right)[F_2(a, b, z) + F_2(a, b, z_0)] \\ & - \mathrm{sgn}(\cos\chi)\sqrt{1 - \gamma^2 u_0^2/\alpha^2}\left[\frac{\pi}{2}(a-b) + F_3(a, b, z) + F_3(a, b, z_0)\right], \end{aligned} \tag{27}$$

$$y(z, \chi, \psi) = -\mathrm{sgn}(\cos\chi)\frac{\sin\psi}{\sqrt{1 - \gamma^2 u_0^2 \cos^2\psi/\alpha^2}}\left[\frac{\pi}{2}(a-b) + F_3(a, b, z) + F_3(a, b, z_0)\right], \tag{28}$$

$$t(z,\chi,\psi) = -\frac{\gamma u_0 \cos\psi\,\mathrm{sgn}(\cos\chi) + \alpha/|\cos\chi|}{\alpha^2\sqrt{1-\gamma^2 u_0^2\cos^2\psi/\alpha^2}} z_0 \left[2\frac{\ln(a+b)}{\sqrt{ab}} + F_1(a,b,z) + F_1(a,b,z_0)\right]$$
$$- \frac{\gamma u_0 \cos\psi\,\mathrm{sgn}(\cos\chi)}{\alpha^2\sqrt{1-\gamma^2 u_0^2\cos^2\psi/\alpha^2}}[F_2(a,b,z) + F_2(a,b,z_0)]. \quad (29)$$

When $\psi = 0$, Eqs. (27)–(29) reduce to their respective 2D counterparts given in Ref. 28.

Figure 1 shows an example of the 3D wavefront originating from a point source at (0, 0, –15 km) and calculated with the 3D HWT algorithm. The surface plot is colored with the initial polar angle values (counted in this case from the vertical downward direction) of the rays, so one can see more clearly that the wavefront is tilted and stretched by the nonuniform flow. Also shown are the positions of the three straight lines — $y = 0$ km, $y = 5$ km and $y = 10$ km — in the plane $z = -25$ km, for which the timefronts shown in Fig. 2 were calculated. Results of numerical calculations obtained with the 3D HWT algorithm are verified with analytical results expressed by Eqs. (19)–(29).

4.2. *Maxwell's "fish-eye" lens*

In this section, we describe a benchmark problem for motionless fluid where, unlike in the benchmark problems considered above, the medium is not a plane-stratified one, but an exact analytic solution for wavefronts can still be found. Geometric optics for this particular inhomogeneous medium was first considered by James Clerk Maxwell in connection with light focusing by optical instruments, and the problem is usually referred to as the Maxwell's "fish-eye" lens.[35]

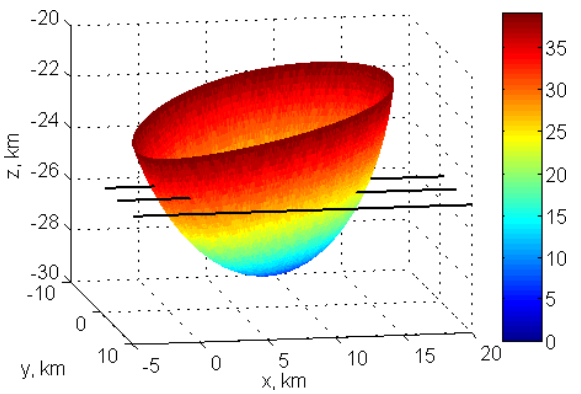

Fig. 1. (Color online) 3D wavefront in a layered medium with linear profiles of the sound speed and the flow velocity. The surface plot shows the wavefront at the travel time $t = 6.5$ sec from a point sound source located at (0 km, 0 km, –15 km). Color scale is employed to show the polar angle at launch from the source of rays arriving at various points on the wavefront. The polar angle is given in degrees, with the zero corresponding to the vertical downward direction. Also shown are the positions of the three straight lines chosen for the timefront calculations presented in Fig. 2. Parameters of the environmental model (17) are $\alpha = 0.1\,\mathrm{sec}^{-1}$, $\gamma = 0.05\,\mathrm{m}^{-1}$ and $u_0 = 0.1\,\mathrm{m}\cdot\mathrm{sec}^{-1}$.

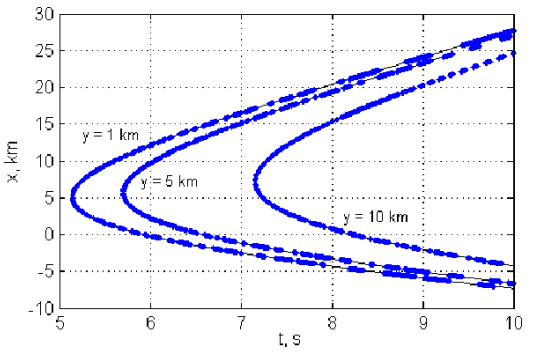

Fig. 2. Timefronts due to a point source in a layered medium with linear profiles of the sound speed and the flow velocity. Geometry of the problem and environmental parameters are the same as in Fig. 1. The timefronts are calculated for three lines $y = 1\,\text{km}$, $5\,\text{km}$ and $10\,\text{km}$ in the plane $z = -25\,\text{km}$, which are shown in Fig. 1. Comparison of analytical calculation based on Eqs. (19)–(29) (solid lines) and numerical calculations with the 3D HWT algorithm employing time steps 0.001 sec (dots) demonstrates an excellent agreement between the two.

Consider an unbounded fluid with quadratic dependence of the sound speed on distance from the origin of coordinates:

$$c = (1 + R^2/a^2)c_0, \quad a > 0. \tag{30}$$

Here R is the magnitude of the position vector $\mathbf{R} = (x, y, z)$ and c_0 is the sound speed at $\mathbf{R} = 0$. The sound speed increases rapidly with R, and the sound can propagate to infinity within finite time. Let a point sound source be located at an arbitrary point $\mathbf{R}_0$. An electromagnetic field due to a point source in a medium, where electric permittivity and magnetic permeability are equal and proportional with a refraction index proportional to $(1 + R^2/a^2)^{-1}$, was considered by Leonhardt and Philbin.[37] The Leonhardt–Philbin electromagnetic problem is kinematically equivalent to sound propagation in fluid with sound speed given by Eq. (30). From high-frequency asymptotics of Eq. (23) in Ref. 37, for the acoustic travel time to point $\mathbf{R}$ we find an explicit expression

$$t = \frac{a}{c_0}\left[(-1)^M \arctan\frac{|\mathbf{R} - \mathbf{R}_0|}{\sqrt{a^2 + 2\mathbf{R}\cdot\mathbf{R}_0 + a^{-2}R^2R_0^2}} + \pi M\right], \quad M = 0, 1, \ldots \tag{31}$$

Equation (31) shows that a radiated pulse returns periodically to every observation point with the same period $T = \pi a/c_0$.

Recalling that the slowness $\mathbf{s} = \boldsymbol{\nabla} t$, it is straightforward to check, without using the results of Ref. 37, that the function (31) satisfies the eikonal equation (1) in the fluid with the sound speed field (30). At $M = 0, t = 0$ at $\mathbf{R} = \mathbf{R}_0$ in Eq. (31), and, hence, Eq. (31) represents timefronts due to a point source at $\mathbf{R} = \mathbf{R}_0$.

Rays in the "fish-eye" lens are arcs of circles; all rays leaving the point $\mathbf{R}_0$ gather at the point

$$\mathbf{R}_1 = -\frac{a^2}{R_0^2}\mathbf{R}_0 \tag{32}$$

and form a perfect focus.[35] After gathering at $\mathbf{R}_1$, rays first diverge and then again converge and form a perfect focus at $\mathbf{R}_0$, and the process repeats periodically. One period is described by giving M two consecutive natural values in Eq. (31).

Equation (31) can be rearranged as an explicit equation for wave fronts:

$$\left|\mathbf{R}+\frac{a^2\mathbf{R}_0}{R_0^2\sin^2\dfrac{c_0t}{a}-a^2\cos^2\dfrac{c_0t}{a}}\right|^2=\frac{a^2(a^2+R_0^2)^2\sin^2\dfrac{2c_0t}{a}}{4\left(R_0^2\sin^2\dfrac{c_0t}{a}-a^2\cos^2\dfrac{c_0t}{a}\right)^2}. \tag{33}$$

This is an equation of a sphere unless $\tan(c_0t/a)=\pm a/R_0$. In the latter case, the sphere degenerates into a plane. At $t=0$, the center of the sphere coincides with the sound source. As t increases, the center moves along the straight line connecting $\mathbf{R}_0$ with the center of symmetry of the medium. (If $\mathbf{R}_0=0$, the center remains fixed, while the radius first increases, becomes infinite, and then decreases to zero.) At $t=(a/c_0)\arctan(a/R_0)$, the center goes to infinity, and the sign of curvature of the wavefront changes. At $t=\pi a/2c_0$, the wavefront collapses into the point $\mathbf{R}=\mathbf{R}_1$. Then the radius of the spherical wavefront increases again, its center moves away from $\mathbf{R}_1$, goes to infinity at $t=(a/c_0)[\pi-\arctan(a/R_0)]$, and starts moving toward $\mathbf{R}_0$. At $t=\pi a/c_0$, the wavefront collapses into the point $\mathbf{R}=\mathbf{R}_0$, and returns to its initial position at $t=0$. At $t>\pi a/c_0$, the process we just described repeats periodically.

Repeated perfect focusing of waves in the Maxwell's "fish-eye" lens presents a particularly stringent test of accuracy of numerical simulations of sound propagation. A comparison between the numerical results obtained using the 3D HWT algorithm and the analytical solution (33) is shown in Fig. 3. The wavefront tracing algorithm accurately reproduces expansion of spherical wavefronts from the point source, their subsequent collapse into a

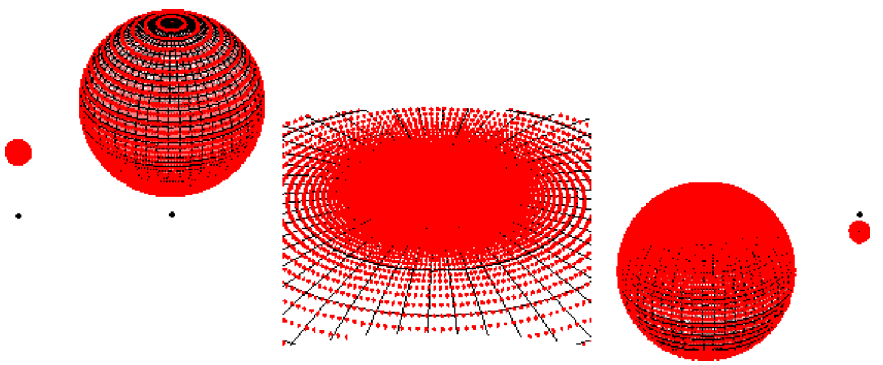

Fig. 3. (Color online) Time evolution of wavefronts in a 3D benchmark problem known as Maxwell's "fish-eye" lens. A numerical solution for wavefronts obtained with the 3D HWT algorithm (red dots) is shown superimposed on the analytical solution (black lines) of the problem. The center of symmetry of the medium is marked with the black dot. The two parameters of the lens are $a=5\,\mathrm{km}$, $c_0=1.5\,\mathrm{km/sec}$; the source shift from the center of symmetry is 10 km. The period of the transient wave field pulsations is $T=10.472\,\mathrm{sec}$. The five panels in the figure correspond to five consecutive steps in the wavefront evolution, covering approximately half of the period: $t/T=0.02, 0.1, 0.15, 0.21, 0.44$ (from left to right).

perfect focus, and the next phase of expansion from the focus followed by collapse into the original sound source. Calculations for longer travel times show that the numerical solution for the wavefronts remains stable and accurate for many periods of the focusing–defocusing process described above.

As was previously illustrated[28] in the case of long-range underwater sound propagation, multiple caustics pose no problems for modeling wavefronts, timefronts and rays with the HWT algorithm. Analysis of the numerical results obtained for the Maxwell's "fish-eye" lens shows that performance of the algorithm is not affected by singularities as strong as the perfect focus.

5. Applications to Ocean and Atmospheric Acoustics

Having verified the validity, stability and accuracy of the numerical wavefront tracing using benchmark problems (Sec. 4), the 3D HWT algorithm was applied to topical problems of long-range sound propagation in the ocean and atmosphere.

5.1. *Acoustic effects due to a packet of nonlinear IWs in shallow water*

In this section, we illustrate possible applications of 3D wavefront tracing to underwater acoustics by considering sound propagation under environmental conditions similar to that of the 1995 Shallow-Water Acoustic Random Media (SWARM) experiment.[38] Rather strong sound speed variations in time and in the horizontal plane were encountered during the SWARM experiment. The sound-speed variability was primarily due to packets of nonlinear IWs, which were generated by tides on a shelfbreak. We follow Refs. 39–42 and use the "dnoidal" model of the vertical isopycnal displacement η in the nonlinear IW packets:

$$\eta(r,z,t) = \eta_0 W(z)\left\{2\mathrm{dn}_s^2\left[\frac{1}{2}k_0(r-Vt)\right] - (1-s^2)\right\} I(r,t)\eta(r,z,t). \tag{34}$$

Here, $\mathrm{dn}_s(\varphi)$ denotes an oscillatory Jacoby elliptic function of argument φ and nonlinear parameter $s(r,t)$; $r(x,y)$ describes the shape of IW fronts in the horizontal plane; $W(z)$ is a shape function of the first normal mode of linear IWs; the amplitude η_0 represents half the peak-to-trough displacement of the leading pulse in the IW packet; V is the nonlinear speed of the soliton and $k_0/2$ is the corresponding wave number.

Assuming a sharp thermocline around depth $z = h_1$, we approximate the shape function of the first IW mode as[39,42] $W(z) = z/h_1$, if $0 < z < h_1$ and $W(z) = (H-z)/(H-h_1)$, if $h_1 < z < H$. In our simulations, we used $h_1 = 20\,\mathrm{m}$, $H = 80\,\mathrm{m}$, the amplitude $\eta_0 = 5\,\mathrm{m}$, nonlinear IW speed $V = 0.63\,\mathrm{m/sec}$, and $k_0 = 0.029\,\mathrm{m}^{-1}$. Parameters of the recovery function[41]

$$I(r,t) = 0.5[1 + \tanh((r - v_0 t - \kappa)/c_0 T_l)]\exp[-a(r-r_0)] \tag{35}$$

are: $v_0 = 0.54\,\mathrm{m/sec}$, $\kappa = 4\,\mathrm{km}$, $T_l = 3\,\mathrm{h}$, $a = 0.02\,\mathrm{km}^{-1}$ and $r_0 = 1\,\mathrm{km}$. We assume that the internal tide is generated by a compact bathymetric feature and let $r(x,y) = [(x-x_0)^2 + (y-y_0)^2]^{1/2}$, where (x_0, y_0) are horizontal coordinates of the center of curvature of the IW fronts.

Following Ref. 42, the sound-speed field in the presence of a strong IW is modeled as

$$c(x, y, z, t) = c_0(x, z + \eta(x, y, z, t)). \tag{36}$$

Here, $c_0(x, z)$ is the range-dependent sound speed[39,40,42] measured in the SWARM experiment. In our simulations, we place the source of sound at the point with coordinates $x = 0, y = 5000\,\text{m}$, $z = 20\,\text{m}$ (i.e. at the depth corresponding to the peak of the first IW mode shape function) and consider two positions for the center of curvature of the IW fronts. With the IW speed being orders of magnitude smaller than the sound speed, we neglect sound-speed variations in time during sound propagation. Put differently, in acoustic wavefront tracing, the sound-speed field is assumed to be "frozen" at the moment of sound radiation. As in Refs. 39, 40 and 42, we also disregard acoustic effects of the fluid flow accompanying IWs compared to the dominant effects due to sound-speed perturbations.

Figure 4 illustrates distortion of acoustic wavefronts by the IW packet at a time when the peak of the sound-speed perturbation reaches the vertical plane $y = 5000\,\text{m}$. Evidence of horizontal refraction of sound can be seen in the upper panel of Fig. 4. IW-induced multi-pathing and apparent "broadening" of timefronts are evident in the lower panel.

Distortions of a particular wavefront, which corresponds to the acoustic travel time of 6 sec, are shown in Fig. 5 for different positions, i.e. stages of evolution, of the IW packet. The IW packet positions are characterized by distance $D = Vt$ the packet covered since its generation; $D = 0$ corresponds to sound propagation in the absence of IWs, while $D = 30\,\text{km}$ corresponds to the time, when the peak of the sound speed distortion reaches

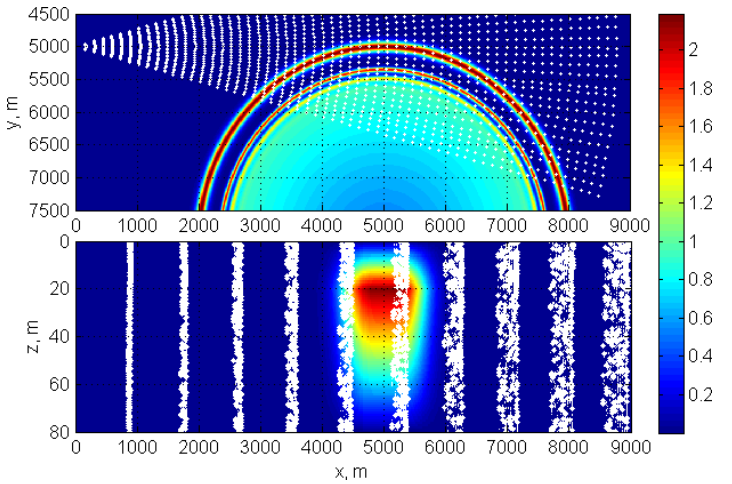

Fig. 4. (Color online) Underwater acoustic wavefronts at propagation through a train of nonlinear IWs. Projections of the wavefronts are shown on the horizontal plane $z = 20\,\text{m}$ (upper panel) and on the vertical plane $y = 5000\,\text{m}$ (lower panel) passing through the sound source located at the point (0 m, 5000 m, 20 m). The internal wave train originates at a location with horizontal coordinates $x = 5000\,\text{m}$, $y = 8000\,\text{m}$. The color scale shows the magnitude of the internal wave-induced displacement (in m) of an isopycnal surface from its unperturbed depth $z = 20\,\text{m}$. White dots show projections of end points of rays, the original distribution of which on the wavefront was uniform, at 10 consecutive times after sound emission by the source.

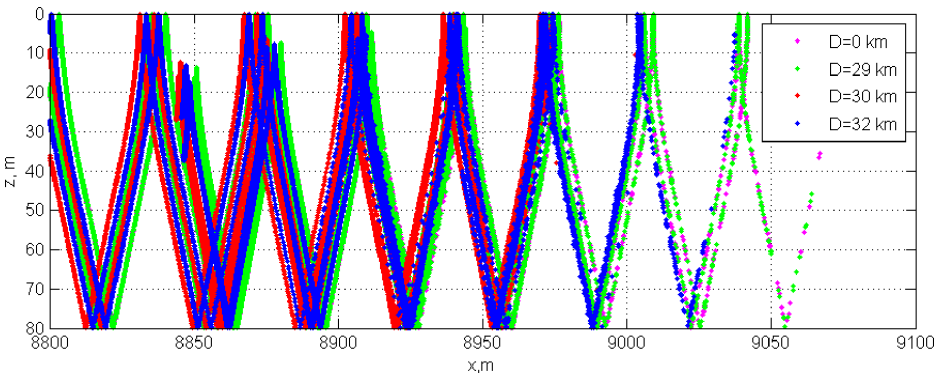

Fig. 5. Evolution of an acoustic wavefront during propagation of a packet of nonlinear internal waves. Cross-section by the vertical plane $y = 5$ km of the acoustic wavefront at travel time $t = 6$ sec is shown for five different stages of the internal wave packet development. A point sound source is located at (0 m, 5000 m, 20 m). The internal wave train originates at a location with horizontal coordinates $x = 5$ km, $y = 35$ km. The packet occupies a circle with radius $D = 0$, 29 km, 30 km, or 32 km. When $D = 0$, sound propagation is unaffected by internal waves. When $D = 30$ km, the maximum of the sound speed perturbations reaches the $y = 5$ km plane.

the $y = 5000$ m plane. Note that the acoustic wavefront maintains its general shape during the IW packet propagation despite strong perturbations of individual rays (not shown) that form the wavefront.

Results of wavefront tracing can be used to determine a number of characteristics of the acoustic field. For some applications, prediction of bearing (i.e. azimuthal) and grazing angles of acoustic arrivals at the receiver are of primary interest. Figure 6 illustrates the effect of the IW packet on the bearing and grazing angles. We have calculated the direction

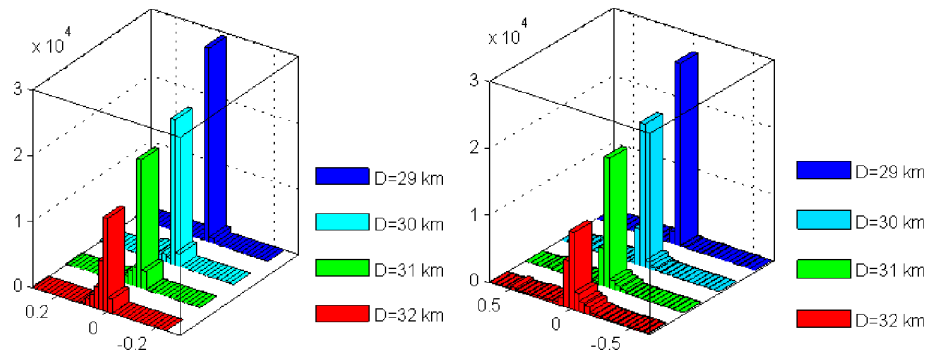

(a) (b)

Fig. 6. Internal wave-induced variations in the direction of sound propagation. Histograms of perturbations (in degrees) in (a) bearing and (b) grazing angles after 6 sec of sound propagation from a point source are shown for four different stages of the nonlinear internal wave packet evolution. Perturbations in the direction of the wave normal are calculated for a section of the acoustic wavefront, which corresponds to azimuthal angles from -5° to 5° and grazing angles from -15° to 15° at the sound source. Geometry of the problem and the meaning of the parameter D are the same as in Fig. 5.

of the wave normal at different points on a particular wavefront for various stages of the IW packet evolution and presented the results as histograms of the bearing and grazing angles perturbations relative to their values in the absence of IWs. As expected, perturbations in the sound propagation direction become stronger, on average, when acoustic rays penetrate deeper into the IW packet (Fig. 6). The width of the distribution for the grazing angle is an order of magnitude larger than of its counterpart for the bearing angle. This is consistent with earlier results,[42] which were obtained by a combination of 2D ray tracing in the vertical plane and a perturbation treatment[43] of the horizontal refraction.

5.2. *Long-range propagation of volcano-generated infrasound*

Relative variations of sound speed in the atmosphere are much larger than in the ocean. Unlike the ocean, where the Mach number of currents, understood as the ratio of the flow velocity to the sound speed, rarely exceeds 10^{-3}, winds can have Mach numbers as large as 0.5 and are a major factor shaping acoustic fields. Combined with strong variations of the sound speed and wind velocity with height, this leads to a rather complicated arrival structure of acoustic fields due to distant compact sources. Understanding and utilizing acoustic arrivals in the atmosphere requires an accurate modeling of sound propagation in moving fluids.[44–47]

Infrasound generated by volcanoes is of particular interest[45,48–50] because the strength of the sound source and its rich low-frequency (below 1 Hz) content ensure detection at hundreds and thousands of kilometers from the source. Moreover, use of observations of volcanic infrasound to monitor winds in the thermosphere has been proposed.[45,48] We illustrate atmospheric applications of the HWT algorithm by modeling propagation of infrasound generated by Eyjafjallajökull volcano in southern Iceland. Eruptions of this volcano were recorded by infrasonic sensors at distances up to 3700 km in 2010.[49]

Modern atmospheric models (for example, the Whole Atmosphere Community Climate Model (WAM)[51,52]) provide information about 3D distributions of all major atmospheric parameters necessary for sound-speed calculations: the temperature T, zonal (u) and meridional (v) components of the wind velocity as well as the content of water vapor and other chemical constituencies. To specify the propagation medium, we used a version of WAM output that provides $\sim 2^\circ$ resolution in geographic coordinates and 150 unevenly distributed grid points in the altitude, from 0 km to 500 km above sea level. Since our main purpose was demonstration of the algorithm capabilities, we did not attempt to match the dates of the WAM output with the dates and times of actual volcano eruptions. However, coordinates of the source, 63°38′N and 19°36′W, and 1.666 km elevation, are quite realistic. Figure 7 illustrates the complicated spatial structure of the horizontal and vertical variations of the physical parameters of the atmosphere that govern infrasound propagation in the Eyjafjallajökull volcano vicinity. It is clear from Fig. 7(c) that variability in horizontal wind is comparable to and can exceed sound-speed variability in a wide range of heights. The vertical component of the wind velocity is usually much smaller than its horizontal component. It is not provided by the WAM model and is assumed to be zero in our simulations. We also

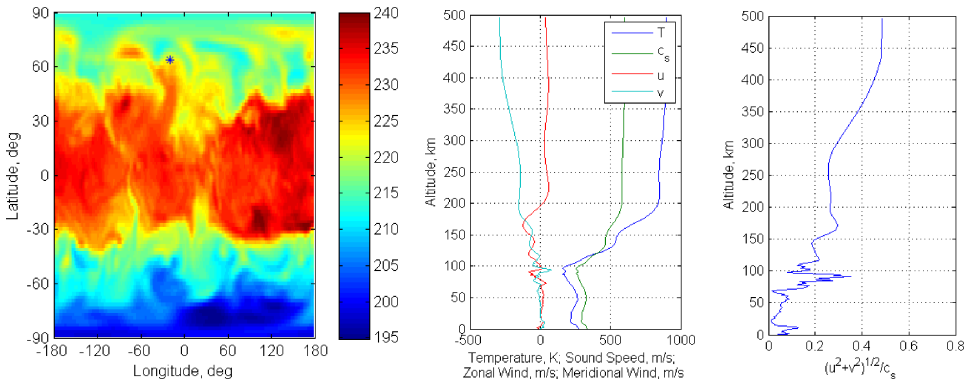

(a) (b) (c)

Fig. 7. Atmospheric model used in simulations of infrasound propagation. (a) Global distribution of the absolute air temperature (in Kelvin) at altitude 10 km predicted by WAM. Eyjafjallajökull, Iceland, location is marked with an asterisk. (b) Vertical profiles of the temperature T, sound speed c, zonal u and meridional v components of wind velocity at the volcano location. (c) Vertical profiles of the Mach number of wind at the volcano location.

disregarded topographic effects and curvature of the Earth and modeled ocean and ground surface as a horizontal plane.

The modified HWT 3D algorithm requires the sound speed and wind velocity in the propagation medium to be set on a uniform 3D grid. The WAM parameters (altitude, temperature and wind components) are given for fixed values of the pressure, geographic latitude and longitude. A standard Matlab interpolation function TriScatteredInterp has been used to convert the WAM output to a grid with constant steps in Cartesian coordinates. Figure 8 presents results of acoustic wavefront and ray calculations using the 3D HWT algorithm and the WAM output in a parallelepiped spanning about 1000 km in horizontal directions and 500 km in the vertical direction. With the origin of coordinates chosen at sea level at the location of the Eyjafjallajökull, horizontal coordinate axes Ox and Oy are directed toward east and north, respectively.

Although not resolved on the scale of the figures, almost all ray paths in Fig. 8(a) and wavefronts in Figs. 8(b) and 8(c) are duplicated because of the reflection from the ground in the vicinity of the elevated sound source. Most of the other peculiarities of the ray and wavefront geometry are due to irregular 3D wind distribution predicted by WAM. Note the very strong anisotropy of infrasound propagation in the horizontal plane, which can be appreciated, in particular, from the shape of a wavefront on the ground (Fig. 8(c)). One can see, for example, downward refraction caused by tropospheric winds at upwind propagation (in the positive direction of the x-axis) (Figs. 8(a) and 8(b)). On the contrary, waves propagating downwind (in the negative direction of the x-axis) are refracted upward, thus creating a shadow zone (Figs. 8(a) and 8(b)). The shadow zone on the ground is terminated by rays turning downward due to strong wind gradients at $\sim$100 km altitudes (Fig. 8(a)).

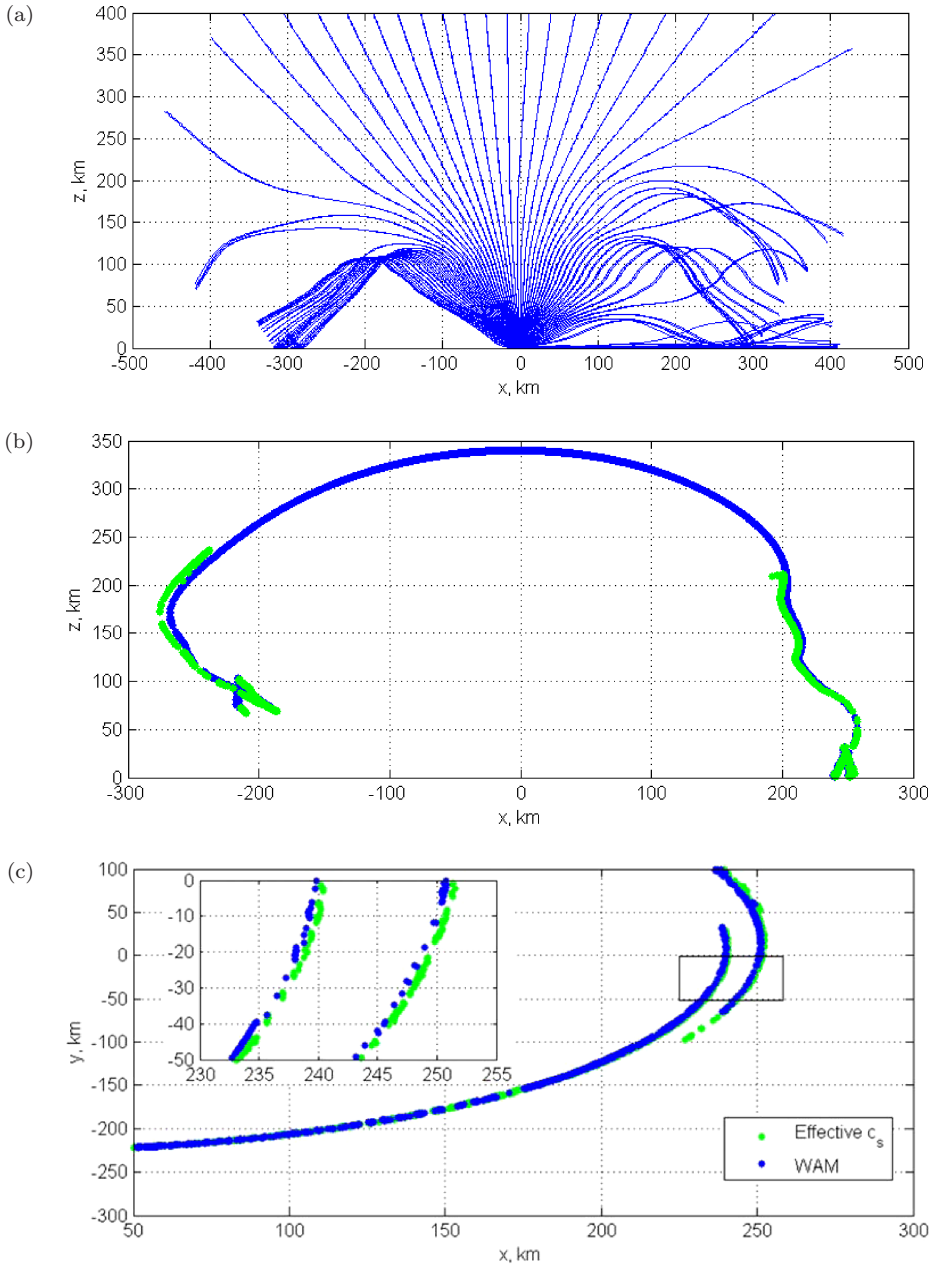

Fig. 8. Application of the 3D HWT algorithm to numerical modeling of infrasound propagation in the atmosphere. (a) Projection on the vertical plane $y = 0$ of rays leaving a point source at the azimuthal angle $\psi = 0$ and with different grazing angles. The point source is placed at the summit of the Eyjafjallajökull volcano at elevation $z_0 = 1666$ m above sea level. (b) Cross-section of the acoustic wavefront at $t = 800$ sec after an eruption by the vertical plane $y = 0$ passing through the source. In addition to the acoustic wavefront in the atmosphere considered as a moving fluid, the result of calculation of the same wavefront in an "effective" motionless fluid is shown. (c) Intersections of the wavefronts shown in (b) with sea and ground surfaces modeled as the horizontal plane $z = 0$. For comparison of the accurate and approximate wavefront calculations, the inset shows a blow-up of a portion of the wavefronts.

The critical role of winds in infrasound propagation demands a careful mathematical description of the effects of the fluid flow on acoustic fields. Effective sound-speed approximation, where a moving medium is replaced by a motionless fluid with an effective sound speed, is widely used in atmospheric acoustics.[45–47] Rays with turning points at and above stratospheric heights encounter very strong winds and may be rather steep in the troposphere, putting the accuracy and validity[53,54] of the effective sound-speed approximation into question. Our HWT algorithm does not rely on the effective sound-speed approximation and allows one to quantify its accuracy.

In the Eyjafjallajökull eruption scenario we consider, the most striking differences between wavefronts in moving and "effective" media are observed at large elevations (Fig. 8(b)). Unlike the actual, moving medium, a large shadow zone arises at near-zenith directions in the "effective" medium. The shadow zone leads to termination of the cross-section of the approximate wavefront at large heights (Fig. 8(b)). Large distortions of the wavefront position occur at intermediate heights. As expected from theoretical analyses[53,54] of the effective sound-speed approximation accuracy, the approximation performs much better for the shallower rays, which are responsible for infrasound arrivals on the ground at $t = 800\,\text{sec}$ (Fig. 8(c)). For the portions of the wavefront shown in the inset in Fig. 8(c), the accurate and approximate wavefronts are separated, on average, by about 1 km, which corresponds to an early arrival bias (i.e. an underestimation of the acoustic travel time) by $\sim 3\,\text{sec}$ in the effective sound-speed approximation.

6. Conclusion

We have developed a numerical implementation of an alternative formulation of the geometrical acoustics, where wavefronts rather than rays are the geometric "backbone" of the wave field. Wavefront tracing can be viewed as a direct implementation of the Huygens' principle. Our wavefront tracing algorithm is an extension to three-dimensionally inhomogeneous, moving media of an earlier 2D algorithm for sound in moving fluids[28] and the original HWT algorithm, developed by Sava and Fomel[23,32] as a part of the open-source Madagascar project for seismic modeling and imaging. Aside from generalization to moving media, the extended HWT algorithm improves the accuracy and stability of the original algorithm, as has been verified through comparisons to exact analytic solutions, and includes new functionality to account for sound reflections at sloping boundaries and to efficiently model acoustic timefronts in addition to the wavefronts.

New benchmark problems have been developed to verify numerical solutions of the eikonal equation against exact analytic solutions. The benchmark problems considered include the Maxwell's "fish-eye" lens, where waves emitted by a point source undergo periodic, perfect focusing, which provides a stringent test of the accuracy and stability of the numerical solutions.

Moving fluids are acoustically anisotropic, and the direction of the normal to the wavefront is generally different from the ray direction. Nevertheless, the HWT algorithm allows one to calculate acoustic rays in moving fluids as a by-product of wavefront tracing. With rays being the paths along which acoustic energy is transported from the sound source, we

find this capability more helpful in interpretation of numerical results in complex inhomogeneous media, such as ocean and atmosphere, than the alternative,[31] where "slowness paths" rather than rays are traced in anisotropic media. While only the specific type of acoustic anisotropy that occurs in moving fluids has been considered in this paper, the approach presented in Sec. 2 can be readily modified to address arbitrary anisotropy.

Within geometric acoustics, the extended HWT algorithm developed in this paper allows one to accurately account for acoustic effects due to atmospheric winds and oceanic currents, as well as 3D refraction and reflection of sound, without any further approximations. The main practical advantage of the wavefront tracing is its computational efficiency, which makes the approach appropriate for solving 3D inverse problems and running 3D Monte Carlo simulations of sound propagation in random media. Computational efficiency of the HWT algorithm also suggests extending it to dispersive waves such as acoustic-gravity waves[55] in the atmosphere. Other possible extensions to be considered in the future include calculation of the wave amplitudes and accounting for sound attenuation.

Acknowledgments

We are grateful to M. Charnotskii for helpful discussions. This research was supported by the Ocean Acoustics Program of the U.S. Office of Naval Research through grant No. N00014-11-1-0048. This work utilized the Janus supercomputer, which is supported by the National Science Foundation (award number CNS-0821794) and the University of Colorado Boulder. The Janus supercomputer is a joint effort of the University of Colorado Boulder, the University of Colorado Denver and the National Center for Atmospheric Research. Janus is operated by the University of Colorado Boulder.

References

1. J. L. Spiesberger, R. C. Spindel and K. Metzger, Stability and identification of ocean acoustic multipaths, *J. Acoust. Soc. Am.* **67** (1980) 2011–2017.
2. T. F. Duda, S. M. Flatté, J. A. Colosi, B. D. Cornuelle, J. A. Hildebrand, W. S. Hodgkiss, P. F. Worcester, B. M. Howe, J. A. Mercer and R. C. Spindel, Measured wavefront fluctuations in 1000-km pulse propagation in the Pacific Ocean, *J. Acoust. Soc. Am.* **92** (1992) 939–955.
3. P. F. Worcester, B. D. Cornuelle, J. A. Hildebrand, W. S. Hodgkiss, T. F. Duda, J. Boyd, B. M. Howe, J. A. Mercer and R. C. Spindel, A comparison of measured and predicted broadband acoustic arrival patterns in travel time–depth coordinates at 1000 km range, *J. Acoust. Soc. Am.* **95** (1994) 3118–3128.
4. P. F. Worcester, B. D. Cornuelle, M. A. Dzieciuch, W. H. Munk, B. M. Howe, J. A. Mercer, R. C. Spindel, J. A. Colosi, K. Metzger, T. Birdsall and A. B. Baggeroer, A test of basin-scale acoustic thermometry using a large-aperture vertical array at 3250-km range in the eastern North Pacific Ocean, *J. Acoust. Soc. Am.* **105** (1999) 3185–3201.
5. O. Witte, M. Roth and G. Müller, Ray tracing in random media, *Geophys. J. Int.* **124** (1996) 159–169.
6. J. Simmen, S. M. Flatté and Guang-Yu Wang, Wavefront folding, chaos, and diffraction for sound propagation through ocean internal waves, *J. Acoust. Soc. Am.* **102** (1997) 239–255.
7. J. A. Colosi, E. K. Scheer, S. M. Flatté, B. D. Cornuelle, M. A. Dzieciuch, W. H. Munk, P. F. Worcester, B. M. Howe, J. A. Mercer, R. C. Spindel, K. Metzger, T. Birdsall and A. B. Baggeroer,

Comparisons of measured and predicted acoustic fluctuations for a 3250-km propagation experiment in the eastern North Pacific Ocean, *J. Acoust. Soc. Am.* **105** (1999) 3202–3218.
8. M. G. Brown, J. A. Colosi, S. Tomsovic, A. L. Virovlyansky, M. A. Wolfson and G. M. Zaslavsky, Ray dynamics in long-range deep ocean sound propagation, *J. Acoust. Soc. Am.* **113** (2003) 2533–2547.
9. F. J. Beron-Vera, M. G. Brown, J. A. Colosi, S. Tomsovic, A. L. Virovlyansky, M. A. Wolfson and G. M. Zaslavsky, Ray dynamics in a long-range acoustic propagation experiment, *J. Acoust. Soc. Am.* **114** (2003) 1226–1242.
10. F. J. Beron-Vera and M. G. Brown, Travel time stability in weakly range-dependent sound channels, *J. Acoust. Soc. Am.* **115** (2004) 1068–1077.
11. D. R. Palmer, T. M. Georges and R. M. Jones, Classical chaos and the sensitivity of the acoustic field to small-scale ocean structure, *Comput. Phys. Commun.* **65** (1991) 219–223.
12. O. A. Godin, Restless rays, steady wavefronts, *J. Acoust. Soc. Am.* **122** (2007) 3353–3363.
13. S. M. Flatté and J. A. Colosi, Anisotropy of the wavefront distortion for acoustic pulse propagation through ocean sound-speed fluctuations: A ray perspective, *IEEE J. Ocean. Eng.* **33** (2008) 477–488.
14. O. A. Godin, Stability of acoustic wave fronts propagating in anisotropic three-dimensional environments, *Acta Acust. United with Acust.* **95** (2009) 963–974.
15. D. Makarov, S. Prants, A. Virovlyansky and G. Zaslavsky, *Ray and Wave Chaos in Ocean Acoustics: Chaos in Waveguides* (World Scientific, Singapore, 2010).
16. J. E. Vidale, Finite-difference calculation of traveltimes in three dimensions, *Geophysics* **55** (1990) 521–526.
17. J. van Trier and W. W. Symes, Upwind finite-difference calculation of travel-times, *Geophysics* **56** (1991) 812–821.
18. V. Vinje, E. Iversen and H. Gjøystdal, Traveltime and amplitude estimation using wavefront construction, *Geophysics* **58** (1993) 1157–1166.
19. S. Gray and W. May, Kirchhoff migration using eikonal equation travel-times, *Geophysics* **59** (1994) 810–817.
20. B. Engquist, E. Fatemi and S. Osher, Numerical resolution of the high frequency asymptotic expansion of the scalar wave equation, *J. Comput. Phys.* **120** (1995) 145–155.
21. J. A. Sethian, *Level Set Methods and Fast Marching Methods Evolving Interfaces in Computational Geometry, Fluid Mechanics, Computer Vision, and Materials Science* (Cambridge University Press, Cambridge, 1999).
22. V. Vinje, K. Åstebøl, E. Iversen and H. Gjøystdal, 3-D ray modeling by wavefront construction in open models, *Geophysics* **64** (1999) 1912–1919.
23. P. Sava and S. Fomel, 3-D traveltime computation using Huygens wavefront tracing, *Geophysics* **66** (2001) 883–889.
24. J. A. Sethian, Evolution, implementation, and application of level set and fast marching methods for advancing fronts, *J. Comput. Phys.* **169** (2001) 503–555.
25. J. D. Benamou, An introduction to Eulerian geometrical optics (1992–2002), *J. Sci. Comput.* **19** (2003) 63–93.
26. J. Qian and S. Leung, A level set based Eulerian method for paraxial multivalued traveltimes, *J. Comput. Phys.* **197** (2004) 711–736.
27. K. Chambers and J.-M. Kendall, A practical implementation of wave front construction for 3-D isotropic media, *Geophys. J. Int.* **173** (2008) 1030–1038.
28. N. A. Zabotin, O. A. Godin, P. C. Sava and L. Y. Zabotina, Acoustic wavefront tracing in inhomogeneous, moving media, *J. Comput. Acoust.* **20** (2012) 1250009-1–1250009-17, doi: 10.1142/S0218396X12500099.

29. S. Martinelli, An application of the level set method to underwater acoustic propagation, *Commun. Comput. Phys.* **12** (2012) 1359–1391, doi: 10.4208/cicp.190311.231211a.
30. S. Martinelli, Numerical boundary conditions for specular reflection in a level-sets-based wavefront propagation method, *Commun. Comput. Phys.* **14** (2013) 509–536, doi: 10.4208/cicp.130312.301012a.
31. Y. Wang, Simultaneous computation of seismic slowness paths and the traveltime field in anisotropic media, *Geophys. J. Int.* **195** (2013) 1141–1148, doi: 10.1093/gji/ggt278.
32. P. Sava and S. Fomel, Huygens wavefront tracing: A robust alternative to conventional ray tracing, *SEP Report* **95** (1997) 101–113.
33. L. M. Brekhovskikh and O. A. Godin, *Acoustics of Layered Media. 2: Point Sources and Bounded Beams*, 2nd edn. (Springer, Berlin, 1999).
34. O. A. Godin and A. G. Voronovich, Fermat's principle for non-dispersive waves in nonstationary media, *Proc. R. Soc. Lond. A* **460** (2004) 1631–1647.
35. M. Born and E. Wolf, *Principles of Optics: Electromagnetic Theory of Propagation, Interference and Diffraction of Light*, 7th edn. (Cambridge University Press, Cambridge, 2002), pp. 157–159.
36. G. A. Korn and T. M. Korn, *Mathematical Handbook for Scientists and Engineers: Definitions, Theorems, and Formulas for Reference and Review* (Dover Publications, Mineola, New York, 2000).
37. U. Leonhardt and T. G. Philbin, Perfect imaging with positive refraction in three dimensions, *Phys. Rev. A* **81** (2010) 011804(R).
38. J. R. Apel, M. Badiey, C.-S. Chiu, S. Finette, R. Headrick, J. Kemp, J. Lynch, A. Newhall, M. Orr, B. H. Pasewark, D. Tielbuerger, A. Turgutt, K. von der Heydt and S. Wolf, An overview of the 1995 SWARM shallow-water internal wave acoustic scattering experiment, *IEEE J. Ocean. Eng.* **22** (1997) 465–500.
39. S. Finette, J. R. Apel, M. Badiey, C.-S. Chiu, R. H. Headrick, J. N. Kemp, J. F. Lynch, A. E. Newhall, K. von der Heydt, B. Pasewark, S. N. Wolf and D. Tielbuerger, Acoustic field variability induced by time evolving internal wave fields, *J. Acoust. Soc. Am.* **108** (2000) 957–972.
40. M. Badiey, Y. Mu, J. Lynch, J. Apel and S. Wolf, Temporal and azimuthal dependence of sound propagation in shallow water with internal waves, *IEEE J. Ocean. Eng.* **27** (2002) 117–129.
41. J. R. Apel, A new analytical model for internal solitons in the ocean, *J. Phys. Oceanogr.* **33** (2003) 2247–2269.
42. O. A. Godin, V. U. Zavorotny, A. G. Voronovich and V. V. Goncharov, Refraction of sound in a horizontally inhomogeneous, time-dependent ocean, *IEEE J. Ocean. Eng.* **31** (2006) 384–401.
43. O. A. Godin, A 2-D description of sound propagation in a horizontally-inhomogeneous ocean, *J. Comput. Acoust.* **10** (2002) 123–151.
44. I. P. Chunchuzov, S. N. Kulichkov, O. E. Popov, R. Waxler and J. Assink, Infrasound scattering from atmospheric anisotropic inhomogeneities, *Izv. Atmos. Ocean. Phys.* **47** (2011) 540–557, doi: 10.1134/S0001433811050045.
45. J. D. Assink, R. Waxler and D. Drob, On the sensitivity of infrasonic traveltimes in the equatorial region to the atmospheric tides, *J. Geophys. Res.* **117** (2012) D01110, doi:10.1029/2011JD016107.
46. A. Le Pichon, L. Ceranna and J. Vergoz, Incorporating numerical modeling into estimates of the detection capability of the IMS infrasound network, *J. Geophys. Res.* **117** (2012) D05121, doi:10.1029/2011JD016670.
47. L. G. Evers, A. R. J. van Geyt, P. Smets and J. T. Fricke, Anomalous infrasound propagation in a hot stratosphere and the existence of extremely small shadow zones, *J. Geophys. Res.* **117** (2012) D06120, doi:10.1029/2011JD017014.

48. A. Le Pichon, E. Blanc, D. Drob, S. Lambotte, J. X. Dessa, M. Lardy, P. Bani and S. Vergniolle, Infrasound monitoring of volcanoes to probe high-altitude winds, *J. Geophys. Res.* **110** (2005) D13106, doi:10.1029/2004JD005587.
49. D. P. Drob, M. Garces, M. Hedlin and N. Brachet, The temporal morphology of infrasound propagation, *Pure Appl. Geophys.* **167** (2010) 437–453.
50. R. S. Matoza, J. Vergoz, A. Le Pichon, L. Ceranna, D. N. Green, L. G. Evers, M. Ripepe, P. Campus, L. Liszka, T. Kvaerna, E. Kjartansson and A. Hoskuldsson, Long-range acoustic observations of the Eyjafjallajökull eruption, Iceland, April–May 2010, *Geophys. Res. Lett.* **38** (2011) L06308.
51. H.-L. Liu, B. T. Foster, M. E. Hagan, J. M. McInerney, A. Maute, L. Qian, A. D. Richmond, R. G. Roble, S. C. Solomon, R. R. Garcia, D. Kinnison, D. R. Marsh, A. K. Smith, J. Richter, F. Sassi and J. Oberheide, Thermosphere extension of the Whole Atmosphere Community Climate Model, *J. Geophys. Res.* **115** (2010) A12302, doi:10.1029/2010JA015586.
52. R. A. Akmaev, Whole atmosphere modeling: Connecting terrestrial and space weather, *Rev. Geophys.* **49** (2011) RG4004, doi:10.1029/2011RG000364.
53. O. A. Godin, D. Yu. Mikhin and S. Ya. Molchanov, On effective sound speed approximation in acoustics of moving media, *Izv. Akad. Nauk. Fiz. Atmos. Okeana* **29** (1993) 194–201.
54. O. A. Godin, An effective quiescent medium for sound propagating through an inhomogeneous, moving fluid, *J. Acoust. Soc. Am.* **112** (2002) 1269–1275.
55. E. E. Gossard and W. H. Hooke, *Waves in the Atmosphere* (Elsevier, Amsterdam, 1975).